A Detailed View of the Broad-line Region in NGC 3783 from Velocity-resolved Reverberation Mapping

Misty C. Bentz[1] , Peter R. Williams[2] , Rachel Street[3] , Christopher A. Onken[4] , Monica Valluri[5] , and Tommaso Treu[2,6]

[1] Department of Physics and Astronomy, Georgia State University, Atlanta, GA 30303, USA; bentz@astro.gsu.edu
[2] Department of Physics and Astronomy, University of California, Los Angeles, CA 90095, USA
[3] LCOGT, 6740 Cortona Drive, Suite 102, Goleta, CA 93117, USA
[4] Research School of Astronomy and Astrophysics, Australian National University, Canberra, ACT 2611, Australia
[5] Department of Astronomy, University of Michigan, Ann Arbor, MI 48104, USA

Abstract

We have modeled the full velocity-resolved reverberation response of the Hβ and He II optical broad emission lines in NGC 3783 to constrain the geometry and kinematics of the low-ionization and high-ionization broad-line region (BLR). The geometry is found to be a thick disk that is nearly face-on, inclined at $\sim 18°$ to our line of sight, and exhibiting clear ionization stratification, with an extended Hβ-emitting region ($r_{median} = 10.07^{+1.10}_{-1.12}$ lt-day) and a more compact and centrally located He II-emitting region ($r_{median} = 1.33^{=+0.34}_{-0.42}$ lt-day). In the Hβ-emitting region, the kinematics are dominated by near-circular Keplerian orbits, but with $\sim 40\%$ of the orbits inflowing. The more compact He II-emitting region, on the other hand, appears to be dominated by outflowing orbits. The black hole mass is constrained to be $M_{BH} = 2.82^{+1.55}_{-0.63} \times 10^7 \, M_\odot$, which is consistent with the simple reverberation constraint on the mass based on a mean time delay, line width, and scale factor of $\langle f \rangle = 4.82$. The difference in kinematics between the Hβ- and He II-emitting regions of the BLR is intriguing given the recent history of large changes in the ionizing luminosity of NGC 3783 and evidence for possible changes in the BLR structure as a result.

Unified Astronomy Thesaurus concepts: Supermassive black holes (1663); Seyfert galaxies (1447); Reverberation mapping (2019)

1. Introduction

Black holes continue to capture our imaginations centuries after the concept was first recorded in a letter written by a country clergyman (Michell 1784). Today, not only are black holes a recurrent feature in science fiction, but they have also become securely ensconced in science fact. We now know that supermassive ($M_{BH} = 10^5$–$10^{10} \, M_\odot$) black holes exist, that they inhabit the centers of most (all?) massive galaxies, and that their masses scale with several measurable properties of their host galaxies, including the bulge stellar velocity dispersion and bulge luminosity (e.g., Magorrian et al. 1998; Ferrarese & Merritt 2000; Gebhardt et al. 2000; Gültekin et al. 2009; Kormendy & Ho 2013).

Only a handful of methods are able to directly constrain the mass of a central, supermassive black hole through its gravitational effects on luminous matter. In the case of the Milky Way, astrometric monitoring of individual stars in the central few parsecs has resulted in a constraint on the mass of Sagittarius A* of $M_{BH} = (4.1 \pm 0.6) \times 10^6 \, M_\odot$ (Ghez et al. 2000; Genzel et al. 2000; Ghez et al. 2008), while relativistic modeling of the emission from gas just outside the event horizon has constrained the mass of Pōwehi, the central black hole in M87, to $M_{BH} = (6.5 \pm 0.7) \times 10^9 \, M_\odot$ (Event Horizon Telescope Collaboration et al. 2019). Most other galaxies are not able to be studied with similar methods because we lack the necessary spatial resolution. However, many nearby galaxies ($D \lesssim 100$ Mpc) may still be studied through spatially resolved observations of the bulk nuclear gas or stellar kinematics on scales of $\sim$tens of parsecs (e.g., Gültekin et al. 2009; Kormendy & Ho 2013). Reverberation mapping is notable

among black hole mass measurement techniques because it relies on time resolution rather than angular resolution. By monitoring the spectrophotometric variability of an active galactic nucleus (AGN), the black hole mass, among other properties, may be constrained for a local Seyfert or a distant quasar (for a recent review, see Cackett et al. 2021).

Reverberation mapping makes use of the response of photoionized gas in the broad-line region (BLR) to variations in the continuum luminosity, a technique that was first proposed by Bahcall et al. (1972). As it is generally implemented, reverberation mapping constrains an average responsivity-weighted radius for the BLR in an AGN. Combining the radius with a measure of the line-of-sight velocity of the BLR gas via the virial theorem constrains M_{BH} (Peterson & Wandel 1999, 2000), modulo a scale factor that accounts for the generally unknown BLR geometry and kinematics (e.g., Onken et al. 2004; Park et al. 2012; Grier et al. 2013; Batiste et al. 2017). However, high-quality spectrophotometric monitoring data contain information about the gas response as a function of line-of-sight velocity, thus providing constraints on the emissivity and position of photoionized gas in a spatially unresolved source (Blandford & McKee 1982). Velocity-resolved reverberation mapping, as it has come to be known, is thus able to directly constrain the BLR geometry and the black hole mass, thus avoiding the need to apply a scale factor.

The analysis of velocity-resolved reverberation mapping data can be approached as an ill-posed inverse problem, in which the goal is to recover the transfer function that describes the time delay distribution as a function of velocity across a broad emission line (e.g., Horne 1994; Skielboe et al. 2015; Anderson et al. 2021). Alternatively, it can be approached through direct modeling, in which a framework of fully self-

---

[6] Packard Fellow.

consistent models is built and an exploration of the available parameter space yields the family of models that best match the observational constraints (e.g., Pancoast et al. 2011). Direct modeling has the advantage that it is relatively simple to interpret the results; however, its ability to match complicated data sets is limited by the phenomenology that is included and how it is parameterized. Recovery of the transfer function, on the other hand, takes advantage of the full range of details present in the observations but is nontrivial to interpret.

While the promise of velocity-resolved reverberation mapping has long been understood, it was only within the past decade or so that improvements in the quality of reverberation mapping data (e.g., Bentz et al. 2008, 2009; Denney et al. 2009; Grier et al. 2012) have finally allowed the BLR structure and kinematics to be explored in detail for a handful of AGNs (Pancoast et al. 2014b; Grier et al. 2017; Williams et al. 2018, 2020). In general, direct modeling has found many similarities across objects, although the exact details vary: the low-ionization BLR is arranged in a thick-disk-like structure at low to moderate inclination to our line of sight, and with kinematics that are dominated by near-circular Keplerian orbits but with a contribution from inflow (although Williams et al. 2018 find evidence for outflow, rather than inflow, in some of their sample). The high-ionization BLR is less well studied, and Williams et al. (2020) find several key differences in not just the kinematics but also the geometry of the low- and high-ionization BLR gas in NGC 5548. Studies that have focused on the recovery of the transfer function have generally drawn similar conclusions about the BLR structure and kinematics (Bentz et al. 2010a; Horne et al. 2021). A key finding of all these studies is that the black hole masses derived from a more simplistic reverberation analysis, involving a mean time delay and line width and an adopted scale factor of $\langle f \rangle \approx 5$, are generally in good agreement within their uncertainties with the masses derived from modeling. As expected, the largest differences are generally found for those AGNs where direct modeling derives an inclination of the BLR that is $\lesssim 15°$ to our line of sight (see Figure 14 of Williams et al. 2018). Very low inclinations result in small observed line-of-sight velocities, which bias the simplistic mass estimates to low values.

We recently conducted a new reverberation mapping program focusing on the bright Southern Seyfert, NGC 3783, with the intent of improving the constraints on the black hole mass. A nearly face-on barred spiral galaxy at $z = 0.0097$, NGC 3783 is one of the most well-studied AGNs in the sky. It is one of a few Seyfert 1 galaxies that may be studied in detail with Very Large Telescope GRAVITY observations on spatial scales that resolve the dust torus and outer BLR (Gravity Collaboration et al. 2021a); thus, it is a critical target for informing our understanding of both feeding and feedback. Furthermore, NGC 3783 is also one of a small number of Seyfert 1 galaxies that are near enough to allow a reverberation-based mass to be directly compared with masses constrained through dynamical methods. The comparison of reverberation and dynamical masses is the only independent check that we can use to investigate the reliability of the entire black hole mass scale that we currently apply across cosmic history, an important point given the different systematic biases that are inherent in each black hole mass measurement technique.

An initial assessment of the monitoring data constrained a reverberation-based black hole mass of $M_{BH} = (2.3 \pm 0.4) \times 10^7 \ M_\odot$ (Bentz et al. 2021), assuming a scale factor of $\langle f \rangle = 4.82$ (Batiste et al. 2017). However, variations in the time delay as a function of velocity across Hβ and other optical emission lines were also seen in the spectra, with longer time delays observed near the line center and shorter time delays in the line wings. These initial results indicated that direct modeling would be likely to provide strong constraints on the BLR geometry and kinematics in NGC 3783, and that we might be able to probe both the low-ionization BLR through the broad Hβ emission line and the high-ionization BLR through the He II $\lambda 4686$ broad line. Here we present the results of that modeling and a new direct constraint on the black hole mass in NGC 3783.

2. Data

A detailed description of the photometric and spectroscopic monitoring data is provided by Bentz et al. (2021). In summary, V-band photometric monitoring was carried out with the Las Cumbres Observatory global telescope (LCOGT) network of 1 m telescopes from 2020 February 12 to June 30. Notwithstanding the sudden onset of a global pandemic and the shutdown of several observatories, 209 images were acquired over this period, with a median temporal sampling of 0.4 days. Spectroscopic monitoring with the robotic FLOYDS spectrograph on the 2 m Faulkes Telescope South was carried out over the same period, with 50 spectra acquired between 2020 February 27 and June 26, with a median temporal sampling of 1.7 days.

The images and spectra were reduced in IRAF[7] following standard procedures. The spectra were intercalibrated using the [O III] $\lambda\lambda 4959$, 5007 emission lines, which are constant in flux on timescales of a few months (Peterson et al. 2013), thus providing a correction for small wavelength shifts, differences in resolution, and offsets in flux calibration from night to night. Image subtraction methods (Alard & Lupton 1998; Alard 2000) were used to isolate the variable AGN point source from the constant host-galaxy emission in the images, providing a well-sampled and well-calibrated light curve of the AGN optical continuum emission. This was merged with the flux-calibrated continuum light curve measured at $5100 \times (1 + z)$ Å in the spectra, with data points taken within 0.25 days binned together for the final continuum light curve.

Before modeling the reverberation response, the continuum and [O III] emission lines were subtracted from each spectrum to allow the broad emission to be isolated. This was accomplished by modeling the spectral components in the high signal-to-noise ratio mean spectrum with ULySS (Koleva et al. 2009) and then slightly adjusting that model to create a best fit for each individual spectrum before subtracting the desired model components. The continuum was fit with a power law, representing the AGN continuum contribution, and a host-galaxy component parameterized by the Vazdekis models derived from the MILES library of empirical stellar spectra (Vazdekis et al. 2010). Emission lines were fit with multiple Gaussian profiles, with four Gaussians needed to match each of the Hβ and [O III] doublet lines and one to four Gaussians needed to match other emission features in the spectrum. Once a best fit was achieved for the mean spectrum,
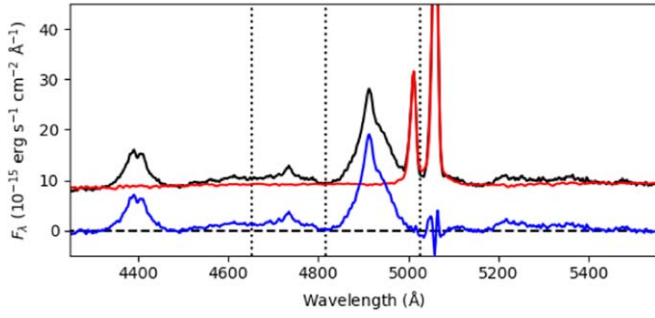
Figure 1. Example spectrum of NGC 3783 in black, with the ULySS fit to the continuum and [O III] $\lambda\lambda 4959, 5007$ doublet overplotted in red and the continuum and O III-subtracted spectrum in blue. The vertical dotted lines mark the limits of the regions that were modeled for the Hβ (4816−5025 Å) and He II (4653−4816 Å) emission lines. With the continuum subtracted, low-level Fe II emission is visible on the blue side of He II and the red side of the [O III] doublet, but the analysis of Bentz et al. (2021) shows that Fe II was not variable at a detectable level in these data.

the individual spectra were then fit one at a time, with the host-galaxy component held fixed to the best-fit template but allowed to vary in flux contribution, and with the power law and the emission-line components allowed to vary but with initial values matching their best-fit values. Once a best fit was found, the host-galaxy and power-law continua and the [O III] components were then subtracted from each spectrum. Figure 1 shows an example spectrum from a single night of observations in black, with the best-fit continuum and [O III] emission in red and the spectrum after subtraction of those components in blue.

The Hβ region was then isolated for modeling between observed wavelengths 4816–5025 Å with the narrow emission line peak at 4910 Å, while the He II region was isolated between 4653 and 4816 Å with the narrow emission line peak observed at 4735 Å. Throughout the campaign, the rest-frame equivalent width of broad Hβ relative to the starlight-corrected AGN continuum has a mean value of 139.9 Å, with a median of 130.5 Å and a standard deviation of 22.4 Å. For He II, the mean rest-frame equivalent width is 15.8 Å, with a median of 15.1 Å and a standard deviation of 5.4 Å. While the blue spectra also cover the Hγ and Hδ broad emission lines and the red spectra cover the Hα emission line, Bentz et al. (2021) described the difficulties in accurately calibrating the red spectra and the short-wavelength end of the blue spectra. The integrated light curves for these emission lines clearly demonstrate significant excess noise, so we do not attempt to model them here.

3. BLR Models

Modeling of the BLR for Hβ and for He II was carried out with CARAMEL, a phenomenological modeling code that is described in detail by Pancoast et al. (2014a). CARAMEL is capable of constraining both the geometry and kinematics of the BLR using the reverberation response across the profile of a broad emission line throughout a monitoring campaign. Here we summarize the main components of the model.

CARAMEL represents the BLR as a large collection of massless point particles that are distributed in position and velocity space, surrounding a massive black hole whose gravity dominates the region. Each point particle processes incident continuum flux instantaneously, and the observed time delay profile of the BLR depends on the spatial distribution of point particles, while the broad-line wavelength profile depends on the velocity distribution of point particles.

The spatial distribution of particles is parameterized with angular and radial distributions. The radial positions of particles are drawn from a gamma distribution

$$p(x|\alpha, \theta) \propto x^{\alpha-1} \exp\left(-\frac{x}{\theta}\right) \quad (1)$$

that provides the flexibility to represent a Gaussian ($\alpha > 1$), an exponential ($\alpha = 1$), or a cuspier profile ($0 < \alpha < 1$). The gamma distribution of particles is shifted away from the location of the black hole by the Schwarzschild radius, $R_s = 2GM/c^2$, plus a minimum radius $r_{\min}$. To assist with interpretation of the modeling results, a change of variables is performed so that parameterization is given in terms of (μ, β, F):

$$\mu = r_{\min} + \alpha\theta, \quad (2)$$

$$\beta = \frac{1}{\sqrt{\alpha}}, \quad (3)$$

$$F = \frac{r_{\min}}{r_{\min} + \alpha\theta}, \quad (4)$$

where μ is the mean radius, β is the shape parameter, and F is $r_{\min}$ in units of μ. The standard deviation of the shifted gamma profile is given by $\sigma_r = \mu\beta(1 - F)$, and the BLR is truncated at an outer radius of $r_{\rm out} = c\Delta t_{\rm data}/2$, where $\Delta t_{\rm data}$ is the time difference between the first point in the modeled continuum light curve and the first point in the emission-line light curve. This truncation assumes that the total length of the monitoring campaign is sufficient to track reverberation signals throughout the entire BLR.

The angular distribution of the particles is then arranged in a disk with a thickness that is set by an opening angle θ_o, where $\theta_o = 0°$ is a thin disk and $\theta_o = 90°$ is a sphere. The inclination of the disk to the observer's line of sight is set by θ_i, where $\theta_i = 0°$ is viewed face-on and $\theta_i = 90°$ is viewed edge-on. The strength of line emission from different depths within the disk is parameterized by the distribution of particles as a function of depth. For a single particle, the angle of displacement from the disk midplane is given by

$$\theta_{d,N} = \arccos(\cos\theta_o + (1 - \cos\theta_o) \times U^\gamma), \quad (5)$$

where U is a random number drawn uniformly between 0 and 1. The value of γ ranges from 1, where particles are distributed uniformly throughout the thickness of the disk, to 5, where particles are clustered at the disk face and therefore emission is preferentially from the outer skin of the BLR. An additional asymmetry parameter, ξ, allows for the possibility of obscuration along the midplane of the disk, where $\xi \to 0$ causes the entire back half of the disk to be obscured and $\xi = 1$ has no midplane obscuration. The final asymmetry parameter κ is related to the weight of a particle

$$W(\phi) = \frac{1}{2} + \kappa\cos\phi, \quad (6)$$

where W is the fraction of continuum flux that is reradiated back toward the observer as line flux and ϕ is the angle between the observer's line of sight to the source and the particle's line of sight to the source. The value of κ ranges from

−0.5, where particles preferentially emit back toward the ionizing source, to 0.5, where particles preferentially radiate away from the ionizing source. In the case of $\kappa = -0.5$, an observer would see preferential emission from the far side of the disk, while preferential emission from the near side would be observed in the case of $\kappa = 0.5$.

The velocity distribution of particles includes radial and tangential distributions. A fraction of the particles, $f_{\rm ellip}$, have near-circular orbits within the Keplerian potential of the central black hole with mass $M_{\rm BH}$. The remaining particles $(1 - f_{\rm ellip})$ are either inflowing $(f_{\rm flow} < 0.5)$ or outflowing $(f_{\rm flow} > 0.5)$. Whether these orbits are generally bound or unbound is determined by the parameter θ_e. For a plane defined by the possible values of the radial and tangential velocities, θ_e describes the angle of the velocity components away from the escape velocity and toward the circular velocity. If $\theta_e = 0°$, then the orbits are drawn from a Gaussian distribution centered on the escape velocity. As $\theta_e \to 90°$, the inflowing or outflowing orbits approach the parameter space occupied by near-circular orbits. Thus, high values of θ_e indicate inflowing or outflowing orbits that are very nearly circular, $\theta_e \approx 45°$ indicates that most of the inflowing or outflowing orbits are highly eccentric but still bound, and low values of θ_e indicate that most particles are near the escape velocity and unbound.

A contribution from macroturbulence is included in the line-of-sight component of the velocity vector for each point particle as

$$v_{\rm turb} = \mathcal{N}(0, \sigma_{\rm turb})|v_{\rm circ}|, \tag{7}$$

where $v_{\rm circ}$ is the circular velocity and $\mathcal{N}(0, \sigma_{\rm turb})$ is a normal distribution centered on 0 and with standard deviation $\sigma_{\rm turb}$.

With the spatial and velocity distributions of the particles parameterized, the emission-line profile can then be calculated for each continuum flux measurement, assuming that the continuum flux tracks the ionizing flux from a central point source. A nonvariable narrow emission line component is included in the modeled emission-line profiles, as is a smoothing parameter to account for the small differences in spectral resolution that arise from variable seeing conditions throughout the monitoring campaign.

To explore the full range of possible time delays arising from the BLR geometry and to properly compare the modeled emission-line profiles with the measured profiles, the continuum light curve must be interpolated. CARAMEL uses Gaussian processes both to interpolate between continuum flux measurements and to extrapolate the continuum light curve beyond the beginning and end of the monitoring campaign to extend the range of time delays that may be probed. The uncertainties on the Gaussian process model parameters are included in the determination of the BLR model parameters, thus capturing the effect of the uncertainties that arise from interpolating and extrapolating the continuum data.

For each model realization, we include 2000 individual point particles to represent the BLR. The continuum light curve is interpolated, and model emission-line profiles are calculated for each epoch at which an emission-line measurement was acquired. A Gaussian likelihood function compares the modeled spectra against the measured spectra and adjusts the model parameters accordingly. CARAMEL utilizes a diffusive nested sampling code, with the latest version employing DNEST4 (Brewer & Foreman-Mackey 2018), to efficiently explore the model parameter space. DNEST4 allows for the use

of a likelihood softening parameter, or statistical temperature T, which has the effect of increasing the measurement uncertainties. This parameter can account for underestimated measurement uncertainties or for the inability of the simplified model to capture all of the real details in the measurements. The value of T is determined in the post analysis by examining the distributions of the model parameters and choosing the largest value of T for which the distributions remain smooth and generally unimodal.

Finally, to check that convergence had been reached, we compared the constrained values of the model parameters from the first half of the model runs to the second half of the model runs, with the total number of model runs being 10,000. There was no discernible difference between the parameters constrained during the first half or second half of the model runs for either Hβ or He II.

4. Results

Modeling of the Hβ emission line in NGC 3783 provides constraints on the low-ionization BLR, while modeling of the He II emission line constrains the high-ionization BLR. Figure 2 compares the posterior probability distribution functions for all the parameters of the BLR models for both Hβ and He II, while the median and 68% confidence intervals for each parameter are listed in Table 1. We describe the resultant set of models for each emission line below.

4.1. Hβ

The models for Hβ require a likelihood softening of $T = 125$, which amounts to increasing the uncertainties on the data by a factor of $\sqrt{T} = 11.2$. Figure 3 displays the continuum and integrated Hβ emission-line light curves and the observed Hβ line profiles along with model fits to all of these. In general, the emission-line profiles are well fit by the modeled profiles, as are the gross flux variations of the integrated emission-line light curve, although some of the finer details of the data are not captured by the models. The small disagreements between the data and the models could be the result of uncertainties that are still underestimated for some data points, or they could signal that the models are too simplistic and do not have the full flexibility needed to match all of the real variations, or both.

The geometry of the Hβ-emitting BLR is found to be a relatively face-on thick disk with an opening angle of $\theta_o = 34.7^{+6.2}_{-9.9}$ deg and an inclination to our line of sight of $\theta_i = 17.9^{+5.3}_{-6.1}$ deg. The disk has an inner minimum radius of $r_{\rm min} = 3.25^{+1.13}_{-1.54}$ lt-day, with a median radius of $r_{\rm median} = 10.07^{+1.10}_{-1.21}$ lt-day and a width of $\sigma_r = 10.47^{+15.44}_{-3.82}$ lt-day. The disk emission is distributed radially in a near-exponential profile $(\beta = 0.95^{+0.25}_{-0.25})$ and is distributed throughout the thickness of the disk with a slight preference for stronger emission near the face of the disk $(\gamma = 1.84^{+1.48}_{-0.67})$ and strong but not total obscuration along the midplane $(\xi = 0.23^{+0.24}_{-0.15})$. The line emission direction is rather unconstrained, with the median value centered around isotropic emission but having large uncertainties that do not discriminate between a preference for radiation toward or away from the central source $(\kappa = 0.04^{+0.31}_{-0.30})$. Figure 4 displays a representative geometric model for the Hβ response in the BLR of NGC 3783, drawn from the posterior probability distribution.

The associated mean and median time delays for Hβ are found to be $\tau_{\rm mean} = 9.05^{+0.68}_{-0.64}$ days and $\tau_{\rm median} = 7.42^{+0.70}_{-0.74}$
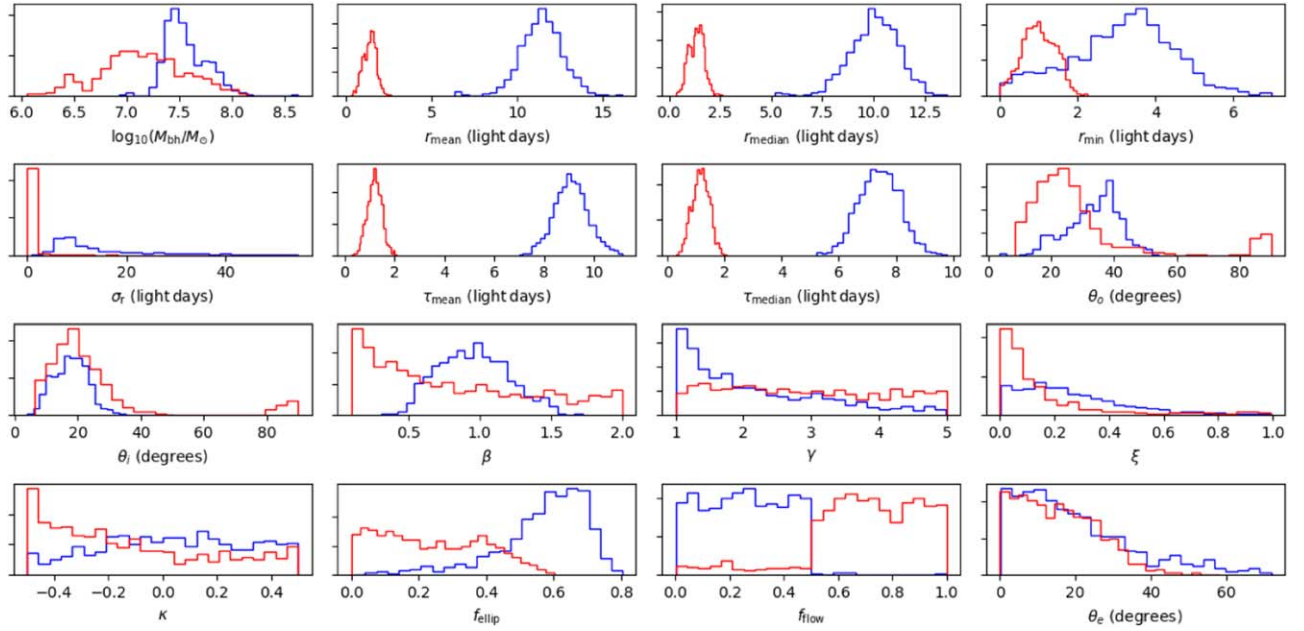
Figure 2. Histograms displaying the posterior distributions of the BLR model parameters for Hβ (blue) and He II (red).

Table 1
Broad-line Region Model Parameter Values

Parameter	Brief Description	Hβ	He II
$\log_{10} (M/M_\odot)$	Black hole mass	$7.51^{+0.26}_{-0.13}$	$7.13^{+0.43}_{-0.37}$
r_{mean} (lt-day)	Mean radius of line emission	$11.41^{+1.13}_{-1.17}$	$1.40^{+0.31}_{-0.42}$
r_{median} (lt-day)	Median radius of line emission	$10.07^{+1.10}_{-1.21}$	$1.33^{+0.34}_{-0.42}$
r_{min} (lt-day)	Minimum radius of line emission	$3.25^{+1.13}_{-1.54}$	$1.00^{+0.46}_{-0.42}$
σ_r (lt-day)	Radial extent of line emission	$10.47^{+15.44}_{-3.82}$	$0.17^{+0.34}_{-0.13}$
τ_{mean} (days)	Mean time delay	$9.05^{+0.68}_{-0.64}$	$1.19^{+0.28}_{-0.30}$
τ_{median} (days)	Median time delay	$7.42^{+0.70}_{-0.74}$	$1.16^{+0.29}_{-0.32}$
θ_o (deg)	Opening angle	$34.7^{+6.2}_{-9.9}$	$23.5^{+11.8}_{-8.0}$
θ_i (deg)	Inclination angle	$17.9^{+5.3}_{-6.1}$	$19.1^{+10.3}_{-7.0}$
β	Shape parameter of radial distribution	$0.95^{+0.25}_{-0.25}$	$0.67^{+0.83}_{-0.45}$
γ	Disk face concentration parameter	$1.84^{+1.48}_{-0.67}$	$2.77^{+1.55}_{-1.23}$
ξ	Transparency of the midplane	$0.23^{+0.24}_{-0.15}$	$0.08^{+0.23}_{-0.06}$
κ	Cosine illumination function parameter	$0.04^{+0.31}_{-0.30}$	$-0.20^{+0.45}_{-0.24}$
f_{ellip}	Fraction of elliptical orbits	$0.60^{+0.09}_{-0.15}$	$0.22^{+0.19}_{-0.16}$
f_{flow}	Inflow versus outflow	$0.26^{+0.17}_{-0.18}$	$0.72^{+0.19}_{-0.17}$
θ_e (deg)	Ellipse angle	$16.1^{+18.6}_{-11.0}$	$14.6^{+11.8}_{-10.3}$
σ_{turb}	Turbulence	$0.024^{+0.050}_{-0.021}$	$0.013^{+0.044}_{-0.011}$
r_{out} (lt-day)	Outer radius of line emission (fixed parameter)	42	42
T	Temperature or likelihood softening	125	145

Note. Tabulated values are the median and 68% confidence intervals.

days, which agree well with the average Hβ time delay reported by Bentz et al. (2021) of $\tau_{cent} = 9.60^{+0.65}_{-0.72}$ days. Figure 5 displays the transfer function, $\Psi(\lambda, \tau)$, for a representative model. Also referred to as the velocity-delay map, the transfer function displays the range of Hβ responsivities as a function of time delay and velocity (or wavelength) across the broad emission line profile. The shape of the transfer function

generally agrees with the cross-correlation time delays computed for different velocity bins of the Hβ profile by Bentz et al. (2021), displayed here as the turquoise crosses in the bottom panel of Figure 5.

The black hole mass is constrained to be $\log_{10}(M_{BH}/M_\odot) = 7.51^{+0.26}_{-0.13}$. Roughly 60% of the particle orbits are near circular ($f_{ellip} = 0.60^{+0.09}_{-0.15}$), with the other 40% strongly preferring inflow ($f_{flow} < 0.5$). With a low value of $\theta_e = 16.1^{+18.6}_{-11.0}$ deg, most of these are truly inflowing orbits rather than highly elliptical bound orbits. There is also a small but nonzero contribution to the kinematics from turbulence ($\sigma_{turb} = 0.024^{+0.050}_{-0.021}$).

4.2. He II

The models for He II require a likelihood softening of $T = 145$, which amounts to increasing the uncertainties on the data by a factor of $\sqrt{T} = 12.0$. Figure 6 displays the continuum and integrated He II emission-line light curves and the observed He II line profiles along with model fits to all of these. In general, the modeled emission-line profiles fit the main features of the observations; however, the lower integrated flux and larger uncertainties compared to Hβ do lead to somewhat less agreement between the observations and the models. The gross flux variations of the integrated emission-line light curve also seem to be mostly captured by the models.

The geometry of the He II-emitting BLR is again found to be a relatively face-on thick disk with an opening angle of $\theta_o = 23.5^{+11.8}_{-8.0}$ deg and an inclination to our line of sight of $\theta_i = 19.1^{+10.3}_{-7.0}$ deg. The disk has an inner minimum radius of $r_{min} = 1.00^{+0.46}_{-0.42}$ lt-day, with a median radius of $r_{median} = 1.33^{+0.34}_{-0.42}$ lt-day and a width of $\sigma_r = 0.17^{+0.34}_{-0.13}$ lt-day. The disk emission is distributed radially in a Gaussian profile ($\beta = 0.67^{+0.83}_{-0.45}$), although the constraints on this parameter are quite weak. The distribution of emission throughout the thickness of the disk is also not well constrained ($\gamma = 2.77^{+1.55}_{-1.23}$), but there is a preference for strong obscuration along the midplane ($\xi = 0.08^{+0.23}_{-0.06}$). The line emission slightly
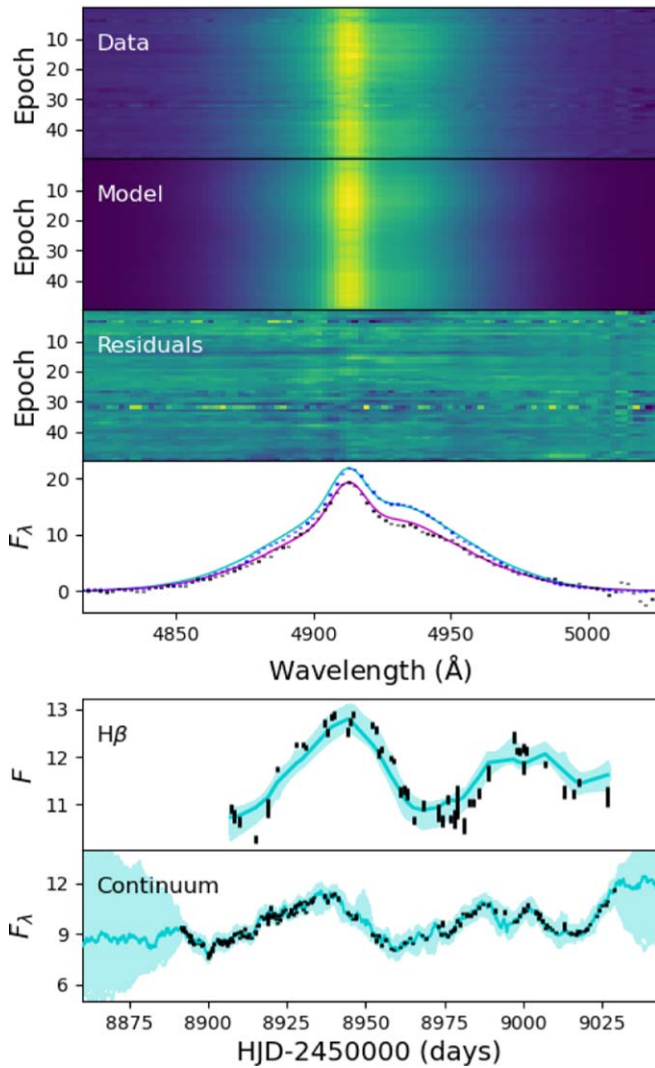
Figure 4. Representative geometric model for the Hβ response in the BLR of NGC 3783, drawn from the posterior probability distribution. The left panel is oriented edge-on, with an Earth-based observer on the $+x$-axis, while the right panel shows the Earth-based observer's view. The transparency of each point represents the relative response of the gas to continuum fluctuations at each position, with more opaque points responsible for a stronger response. This effect is most easily viewed in the right panel, where there is less overlap between points.

Figure 3. The top three panels display the data, one possible model, and residuals (data−model) for the Hβ spectra, with epochs 1 and 13 and their model fits displayed immediately below to exemplify a low flux spectrum (magenta curve) and a high flux spectrum (cyan curve). The bottom two panels display the continuum and integrated Hβ light curves as data points with model fits overlaid. The full ranges of the models are displayed in light turquoise, with the example model corresponding to the top four panels overlaid in dark turquoise. Flux densities (F_λ) are in units of 10^{-15} erg s^{-1} cm^{-2} Å^{-1}, while integrated flux (F) is in units of 10^{-13} erg s^{-1} cm^{-2}. Across the six panels, it is evident that most of the gross characteristics of the data are captured by the models, although some of the finer details are not. Furthermore, the continuum model is less well constrained during time periods with multiday gaps between the measurements. Unfortunately, these gaps resulted from the shutdown of numerous observatories in response to the global coronavirus pandemic and could not be avoided.

Figure 5. Transfer function $\Psi(\lambda, \tau)$ for the example Hβ model displayed in Figure 4. Integrating the transfer function over wavelength gives the one-dimensional lag profile $\Psi(\tau)$, which is shown on the right. Integrating the transfer function over time delay gives $\Psi(\lambda)$, or the variable emission-line profile, which is shown immediately under the transfer function. The bottom panel displays the average lag as a function of wavelength across the emission line, with the turquoise crosses showing the average time delay for five velocity bins across the Hβ profile from Figure 6 of Bentz et al. (2021).

prefers radiation back toward the central source ($\kappa = -0.20^{+0.45}_{-0.24}$). Figure 7 displays a representative model for the He II response in the BLR of NGC 3783, drawn from the posterior probability distribution. As expected, it is significantly more compact than Hβ.

The associated mean and median time delays for He II are found to be $\tau_{\rm mean} = 1.19^{+0.28}_{-0.30}$ days and $\tau_{\rm median} = 1.16^{+0.29}_{-0.32}$ days, which are a bit more compact but agree within the uncertainties with the average He II time delay reported by Bentz et al. (2021) of $\tau_{\rm cent} = 1.95^{+1.02}_{-0.98}$ days. Figure 8 displays the transfer function for a representative model. The shape is much more as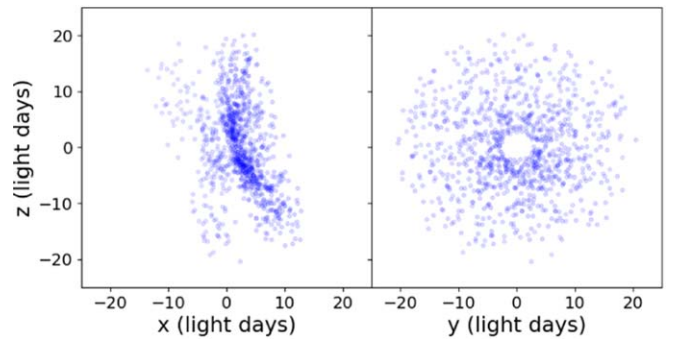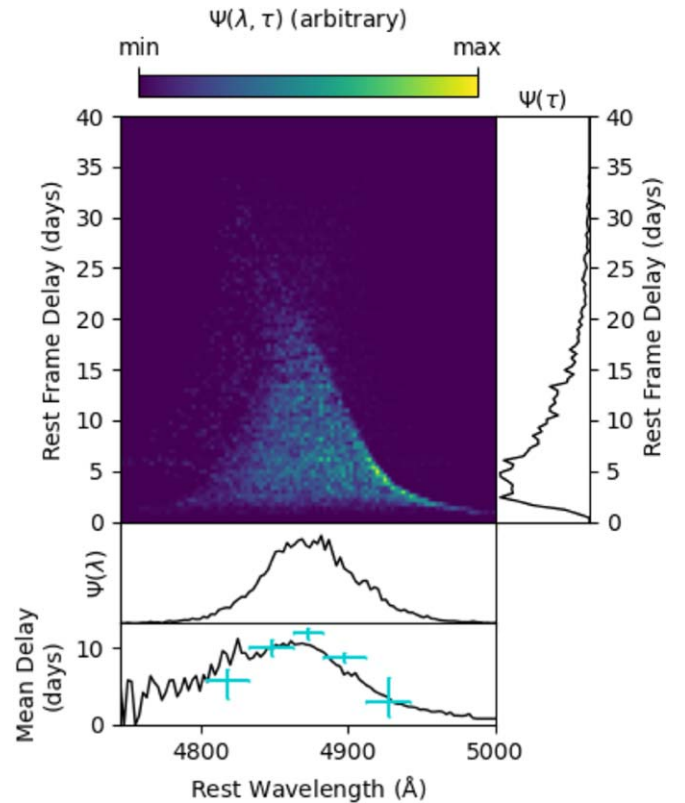ymmetric than was found for Hβ, with a heavier response in the blue wing and very little response in the red wing.

The black hole mass is constrained to be $\log_{10}(M_{\rm BH}/M_\odot) = 7.13^{+0.43}_{-0.37}$. Only 1/5 of the particle orbits are near circular ($f_{\rm ellip} = 0.22^{+0.19}_{-0.16}$), while the rest of the orbits strongly prefer outflow ($f_{\rm flow} > 0.5$). With a low value of $\theta_e = 14.6^{+11.8}_{-10.3}$ deg, most of these are truly outflowing orbits
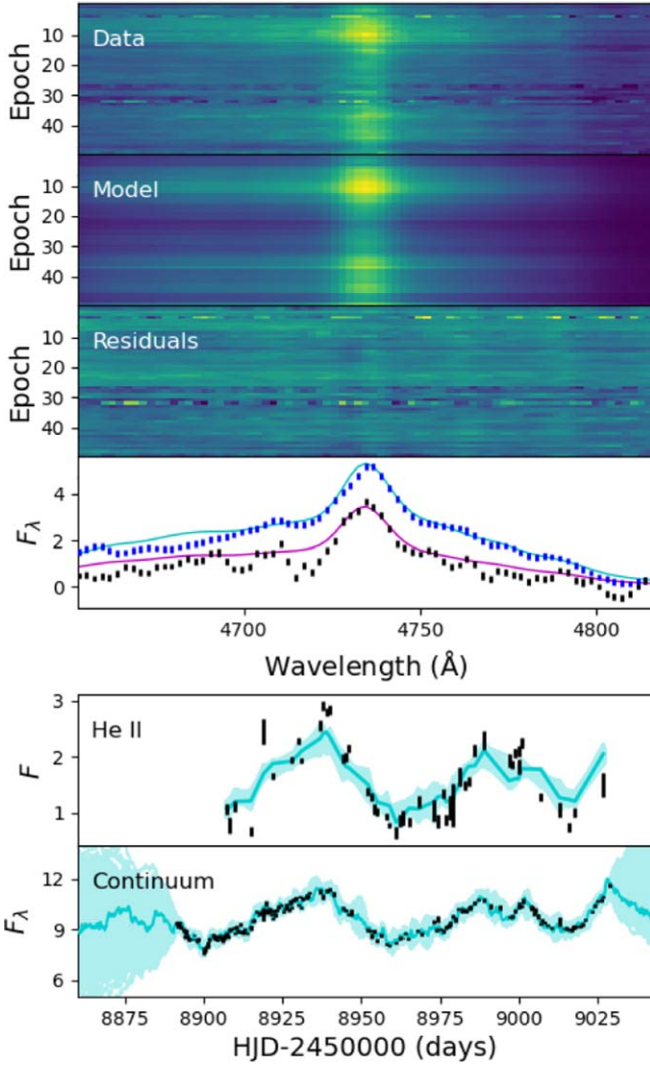
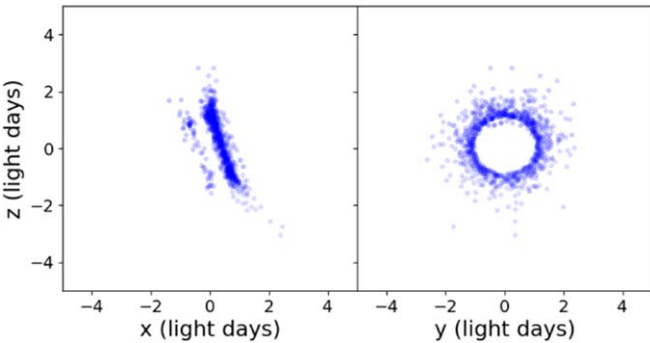**Figure 6.** Same as Figure 3, but for He II.

Figure 7. Same as Figure 4, but for He II.

rather than highly elliptical bound orbits. Finally, there is again a small but nonzero contribution to the kinematics from turbulence ($\sigma_{\mathrm{turb}} = 0.013^{+0.044}_{-0.011}$).

5. Discussion

While both emission lines were modeled independently, they arise from the same AGN and should agree on some parameters while possibly differing for others. Comparing and contrasting
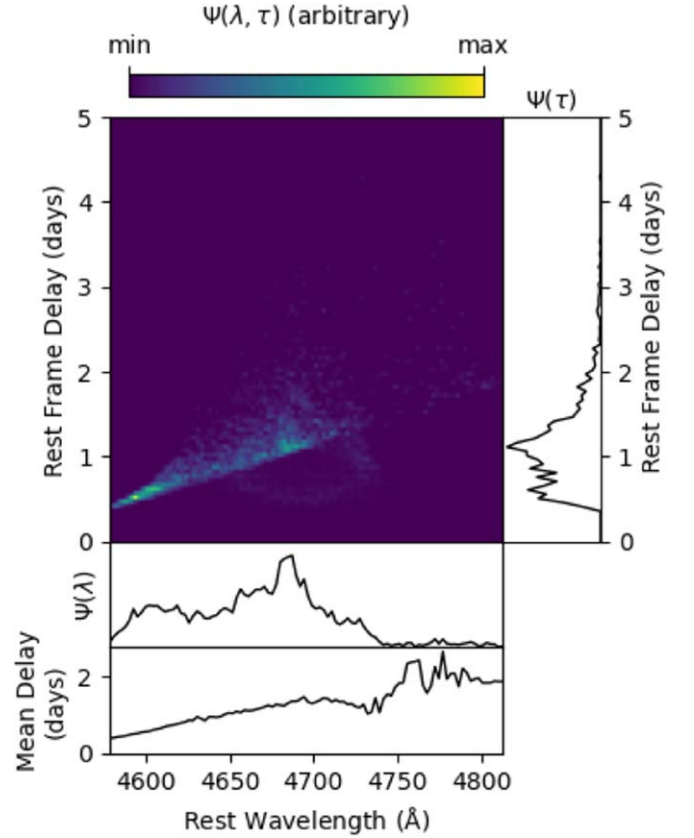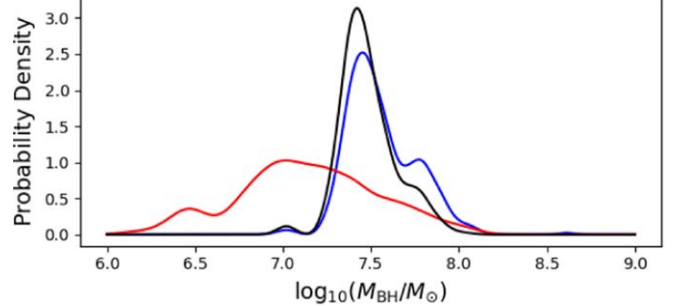

Figure 8. Same as Figure 5, but for He II.

Figure 9. Constraints on the black hole mass in NGC 3783 from Hβ (blue), He II (red), and the joint inference using results from both emission lines (black).

the results for Hβ and He II in the context of other studies may thus shed additional light on the Seyfert nucleus of NGC 3783.

5.1. Black Hole Mass

The black hole mass of NGC 3783 is expected to be the same for both Hβ and He II. And indeed, we see that there is significant overlap between the two in the top left panel of Figure 2. We investigated the joint inference on the black hole mass following the method described by Williams et al. (2020). We first approximated the posterior probability distribution functions of each with a Gaussian kernel density estimate and then multiplied them together. The result is shown in Figure 9 and gives $\log_{10}(M_{\mathrm{BH}}/M_\odot) = 7.45^{+0.19}_{-0.11}$, or $M_{\mathrm{BH}} = 2.82^{+1.55}_{-0.63} \times 10^7 \ M_\odot$. This is consistent with the simple reverberation constraint on the mass, $M_{\mathrm{BH}} = 2.34^{+0.43}_{-0.43} \times 10^7 \ M_\odot$, or $\log_{10}(M_{\mathrm{BH}}/M_\odot) = 7.37^{+0.07}_{-0.09}$, which is based on the

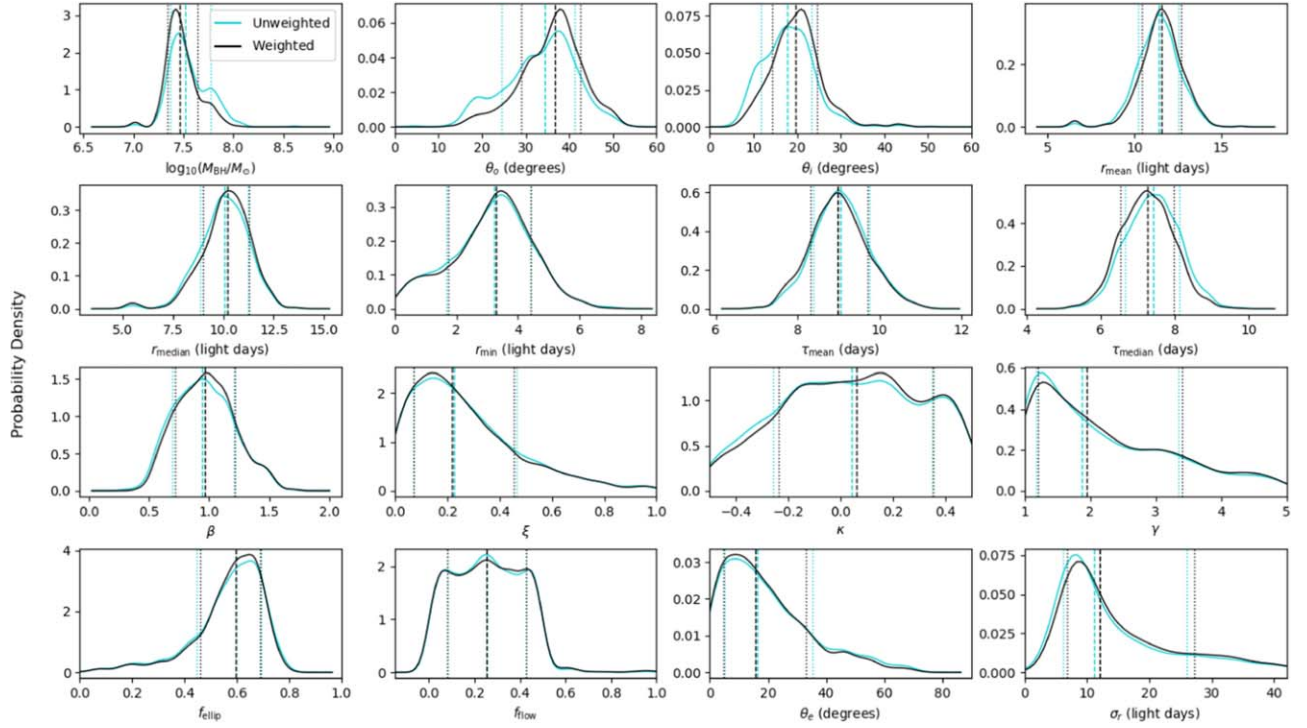**Figure 10.** Posterior distributions of the BLR model parameters for Hβ before (turquoise, "unweighted") and after (black, "weighted") selecting only those models that agree with the joint constraint on M_{BH}. The unweighted distributions in turquoise are the same as the results for Hβ in Figure 2 but are effectively smoothed with a Gaussian kernel for easier comparison with the weighted constraints. The vertical dotted lines mark the median values, while the dashed vertical lines mark the 68% confidence intervals. The parameters are generally unchanged when models that agree with the joint constraint on M_{BH} are preferred.

mean Hβ time delay and line width and an assumed scale factor of $\langle f \rangle = 4.82$. We note that the uncertainties quoted for the simple mass constraint include only the measurement uncertainties on the time delay and line width and do not include other potential uncertainties such as the object-to-object variation in the scale factor.

With a black hole mass constraint from the BLR models, we can infer a specific value of $f = 6.0^{+3.5}_{-1.8}$ for NGC 3783 using the mean time delay and line width for Hβ. Previous investigations (Pancoast et al. 2014b; Grier et al. 2017; Williams et al. 2018) have found that f scales most strongly with the inclination of the system, as expected because only the line-of-sight velocity component is measured. NGC 3783 seems to follow the same trend that has previously been seen for other Seyfert galaxies, as the inclination angle constrained by the models, together with the linear regression results of Williams et al. (2018), predicts $f = 6^{+16}_{-4}$, or $\log_{10}(f) = 0.75^{+0.59}_{-0.61}$. Thus, the good agreement between our mass constraint and the simple reverberation constraint arises from the inclination of NGC 3783 being close to the mean inclination value for the sample of local Seyfert galaxies, thus having an individual f factor that is similar to the population average.

We can also investigate any changes to the distributions of model parameters that may arise from selecting only those models that agree with the joint Hβ and He II constraint on M_{BH}. Figure 10 shows the constraints on the model parameters for Hβ before and after selecting only those models that agree with the joint M_{BH} constraint. The results are quite similar, which is unsurprising since the Hβ models provided the strongest initial constraint on M_{BH}. Figure 11 shows the same but for He II. In this case, we find that models that favor the joint constraint on M_{BH} also favor a slightly larger radius,

which makes sense since the joint constraint on M_{BH} was at the upper end of the M_{BH} mass distribution for He II and also favors an even smaller fraction (~15%) of bound near-circular orbits with the rest of the orbits outflowing. No additional changes are seen in the distributions of the model parameters if we similarly constrain the inclination angle in addition to M_{BH}, in which case we find a joint constraint of $\theta_i = 18.2^{+3.6}_{-5.5}$ deg.

5.2. Geometry and Kinematics

The similarities between the inclinations and opening angle constraints for Hβ and He II support the interpretation that both emission lines are probing different regions of the same thick disk of gas. While the median values of the opening angles might suggest that the Hβ-emitting region is more "puffed up" than the He II-emitting region, as might be expected for a bowl-shaped model of the BLR like that proposed by Goad et al. (2012), the large uncertainties on the He II opening angle mean that the two values formally agree. As expected from the differences in their mean time delays reported by Bentz et al. (2021), the He II-emitting region is significantly more compact and close to the central ionizing source than the Hβ-emitting region, demonstrating clear ionization stratification within the BLR (e.g., Peterson 1993 and references therein). There is little to no overlap between the two, with $r_{min} = 3.25^{+1.13}_{-1.54}$ lt-day for Hβ compared to $r_{mean} = 1.40^{+0.31}_{-0.42}$ lt-day and $\sigma_r = 0.17^{+0.34}_{-0.13}$ lt-day for He II (see Figure 12).

The two regions of the BLR appear, however, to be dominated by different kinematics. In the case of the Hβ-emitting region, the kinematics are dominated by near-circular orbits with some infall, whereas the He II-emitting region is dominated by outflow. Repeated studies of the same AGN, such as NGC 5548 (Pancoast et al. 2014b; Williams et al.
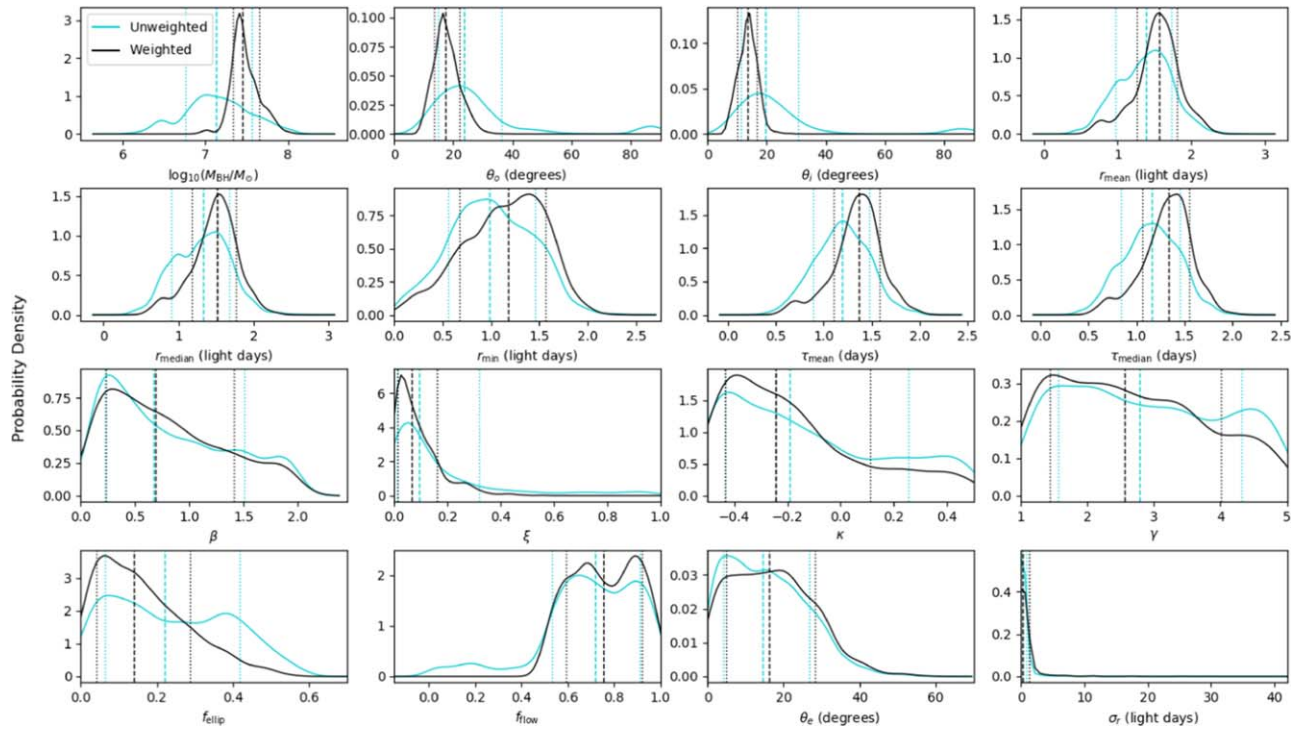
Figure 11. Same as Figure 10, but for He II. The most significant changes are for the BLR radius, which shifts to larger values, and the fraction of near-circular orbits, which decreases to smaller values.
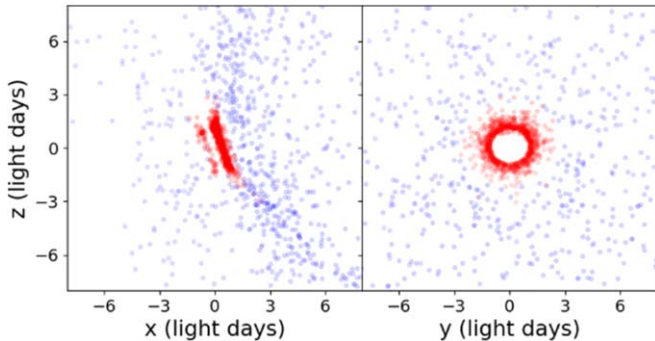

Figure 12. Combined representative geometric models for the Hβ response (blue) and He II response (red) in the BLR of NGC 3783. The left panel is oriented edge-on, with an Earth-based observer on the $+x$-axis, while the right panel shows the Earth-based observer's view. The transparency of each point represents the relative response of the gas to continuum fluctuations at each position, with more opaque points responsible for a stronger response.

2020), have found that the best-fit kinematics can change from one reverberation data set to another, so the different kinematics may not be indicating structural differences between the inner and outer BLR in NGC 3783, but rather transient effects ("weather"). On the other hand, Korista & Goad (2004) find that photoionization models predict that He II λ4686 is preferentially emitted in the presence of an ionizing photon flux that is $\sim$300 times stronger than Hβ. While Hβ-emitting gas in the BLR has been shown to be fairly stable against radiation pressure (Netzer & Marziani 2010), He II is preferentially emitted from lower-density gas (Korista & Goad 2004) and may be more susceptible to radiation pressure forces.

It may be that a combination of weather and photoionization physics explains the difference in kinematics between Hβ and He II. NGC 3783 has demonstrated possible evidence for changes in the structure of the BLR in the recent past. Kriss

et al. (2019) obtained UV spectra of NGC 3783 shortly after the discovery of a strong soft X-ray obscuring event was detected in 2016. They interpret changes in the UV broad emission lines of NGC 3783, together with the appearance of new broad absorption lines, as evidence that the BLR scale height may have collapsed following a period of low ionizing luminosity that began in 2013 and continued to 2016. By late 2016, the luminosity had increased significantly and remained high through at least 2018 January (Kaastra et al. 2018) and could thus begin to drive changes in the structure of the BLR on the dynamical timescale ($\sim$0.3 yr at a BLR radius of 2.0 lt-day, or 3 yr at a radius of 10 lt-day). The luminosity of NGC 3783 between early 2018 and early 2020, when our observing campaign began, is unknown, but the BLR may have still been in the process of recovering from the extended low-luminosity period observed in 2013–2016. And, indeed, a rough comparison of the broad Hβ profile in 2020 with the profiles observed in 2011 and 2016 (Figure 18; Kriss et al. 2019) suggests that much of the flux deficit observed in the line core in 2016 has filled in, although the line profile has not fully returned to its 2011 state. Further multiwavelength monitoring coupled with velocity-resolved reverberation analyses could help to inform our understanding of structural changes in the BLR as a result of large changes in the ionizing luminosity.

Several studies of NGC 3783 have focused on attempts to model the accretion disk using the Fe Kα emission line or the continuum emission (Brenneman et al. 2011; Patrick et al. 2011; Capellupo et al. 2017) and have found similar relatively face-on inclinations for the inner accretion disk, even when they disagree on other components of the models (such as the black hole spin). A similar inclination angle has also been found by modeling the three-dimensional structure of the spatially resolved narrow-line region on parsec scales (Fischer et al. 2013). The consistency in inclination angles from the

innermost regions of the accretion disk through the BLR and the outermost narrow-line region suggests that the spin axis of the central black hole has been stable for quite some time. With no evidence for large torques on the spin, and with the black hole spin axis apparently matching the rotation axis of this relatively face-on galaxy, the recent evolution of the super-massive black hole appears to be dominated by secular processes that are aligned with the disk of the galaxy.

The best-fit models that we find for $H\beta$ also agree well with recent interferometry results for NGC 3783 from GRAVITY (Gravity Collaboration et al. 2021a), in which measurements of the broad $Br\gamma$ emission are best described by a rotating thick disk inclined at $\sim20°$ to our line of sight and surrounding a black hole with $\log_{10}(M_{BH}/M_\odot) = 7.68^{+0.45}_{-0.43}$. Additionally, the radial extent of the $Br\gamma$-emitting region ($r_{mean} = 16^{+12}_{-5}$ lt-day assuming $D = 38.5$ Mpc) is in good agreement with the radial extent of the $H\beta$-emitting region ($r_{mean} = 11.4^{+1.1}_{-1.1}$ lt-day; see Table 1). A joint analysis of the GRAVITY observations with the continuum and integrated $H\beta$ light curves from Bentz et al. (2021) confirms and improves on the results, with $M_{BH} = 2.54^{+0.90}_{-0.72} \times 10^7$ $M_\odot$, or $\log_{10}(M_{BH}/M_\odot) = 7.40^{+0.13}_{-0.14}$, and $r_{median} = 16.2^{+2.8}_{-1.8}$ lt-day (Gravity Collaboration et al. 2021b). The black hole mass is still in excellent agreement with our findings, while the stronger constraints on the BLR radius in the joint analysis are somewhat in tension with the size of the BLR reported here ($r_{median} = 10.07^{+1.10}_{-1.21}$ lt-day). It is important to recognize that the GRAVITY results depend on the distance to NGC 3783, which is somewhat uncertain (recent studies suggest values of 35–50 Mpc; Kourkchi et al. 2020; Robinson et al. 2021); reverberation mapping measures a responsivity-weighted radius, while interferometry measures a flux-weighted radius; and photoionization effects (which are ignored in both our models and those employed in the analysis of the GRAVITY data) are known to cause different reverberation time delays for different hydrogen recombination lines (e.g., Bentz et al. 2010b). Despite these complicating factors, the good agreement between the results lends additional confidence to both. Future work will investigate the joint constraints that may be derived from an analysis of the velocity-resolved reverberation data that we have presented here in tandem with the GRAVITY observations.

6. Summary

We have modeled the full velocity-resolved response of the broad $H\beta$ and He II emission lines in NGC 3783. The results give a black hole mass constraint that is independent of any scaling factor, and a joint analysis of the results for the two emission lines prefers $M_{BH} = 2.82^{+1.55}_{-0.63} \times 10^7$ $M_\odot$. The geometry of the BLR is found to be a thick disk that is close to face-on ($\theta_i \approx 18°$) and exhibiting clear ionization stratification, with $H\beta$ arising from an extended region of ~3–20 lt-day, while He II arises from a significantly more compact and centralized region of 1–2 lt-day. The kinematics of the outer BLR probed by $H\beta$ are dominated by near-circular orbits with a contribution from infall, whereas the kinematics of the inner BLR probed by He II are dominated by an unbound outflow. Given the recent history of a deficit of ionizing radiation in NGC 3783 that was observed from 2013 to 2016 and the hypothesis that the BLR height collapsed as a result, it is possible that we may be seeing the BLR undergoing structural changes as it recovers.

ORCID iDs

Misty C. Bentz https://orcid.org/0000-0002-2816-5398
Peter R. Williams https://orcid.org/0000-0002-4645-6578
Rachel Street https://orcid.org/0000-0001-6279-0552
Christopher A. Onken https://orcid.org/0000-0003-0017-349X
Monica Valluri https://orcid.org/0000-0002-6257-2341
Tommaso Treu https://orcid.org/0000-0002-8460-0390

References

Alard, C. 2000, A&AS, 144, 363
Alard, C., & Lupton, R. H. 1998, ApJ, 503, 325
Anderson, M. D., Baron, F., & Bentz, M. C. 2021, MNRAS, 505, 2903
Bahcall, J. N., Kozlovsky, B.-Z., & Salpeter, E. E. 1972, ApJ, 171, 467
Batiste, M., Bentz, M. C., Raimundo, S. I., Vestergaard, M., & Onken, C. A. 2017, ApJL, 838, L10
Bentz, M. C., Horne, K., Barth, A. J., et al. 2010a, ApJL, 720, L46
Bentz, M. C., Street, R., Onken, C. A., & Valluri, M. 2021, ApJ, 906, 50
Bentz, M. C., Walsh, J. L., Barth, A. J., et al. 2009, ApJ, 705, 199
Bentz, M. C., Walsh, J. L., Barth, A. J., et al. 2010b, ApJ, 716, 993
Bentz, M. C., Walsh, J. L., Barth, A. J., et al. 2008, ApJL, 689, L21
Blandford, R. D., & McKee, C. F. 1982, ApJ, 255, 419
Brenneman, L. W., Reynolds, C. S., Nowak, M. A., et al. 2011, ApJ, 736, 103
Brewer, B. J., & Foreman-Mackey, D. 2018, J. Stat. Softw., 86, 1
Cackett, E. M., Bentz, M. C., & Kara, E. 2021, iSci, 24, 102557
Capellupo, D. M., Wafflard-Fernandez, G., & Haggard, D. 2017, ApJL, 836, L8
Denney, K. D., Peterson, B. M., Pogge, R. W., et al. 2009, ApJL, 704, L80
Event Horizon Telescope Collaboration, Akiyama, K., Alberdi, A., et al. 2019, ApJL, 875, L6
Ferrarese, L., & Merritt, D. 2000, ApJL, 539, L9
Fischer, T. C., Crenshaw, D. M., Kraemer, S. B., & Schmitt, H. R. 2013, ApJS, 209, 1
Gebhardt, K., Bender, R., Bower, G., et al. 2000, ApJL, 539, L13
Genzel, R., Pichon, C., Eckart, A., Gerhard, O. E., & Ott, T. 2000, MNRAS, 317, 348
Ghez, A. M., Morris, M., Becklin, E. E., Tanner, A., & Kremenek, T. 2000, Natur, 407, 349
Ghez, A. M., Salim, S., Weinberg, N. N., et al. 2008, ApJ, 689, 1044
Goad, M. R., Korista, K. T., & Ruff, A. J. 2012, MNRAS, 426, 3086
Gravity Collaboration, Amorim, A., Bauböck, M., et al. 2021a, A&A, 648, A117
Gravity Collaboration, Amorim, A., Bauböck, M., et al. 2021b, arXiv:2107.14262
Grier, C. J., Martini, P., Watson, L. C., et al. 2013, ApJ, 773, 90
Grier, C. J., Pancoast, A., Barth, A. J., et al. 2017, ApJ, 849, 146
Grier, C. J., Peterson, B. M., Pogge, R. W., et al. 2012, ApJ, 755, 60
Gültekin, K., Richstone, D. O., Gebhardt, K., et al. 2009, ApJ, 698, 198
Horne, K. 1994, in ASP Conf. Ser., 69, Reverberation Mapping of the Broad-Line Region in Active Galactic Nuclei, ed. P. M. Gondhalekar, K. Horne, & B. M. Peterson (San Francisco, CA: ASP), 23
Horne, K., De Rosa, G., Peterson, B. M., et al. 2021, ApJ, 907, 76
Kaastra, J. S., Mehdipour, M., Behar, E., et al. 2018, A&A, 619, A112
Koleva, M., Prugniel, P., Bouchard, A., & Wu, Y. 2009, A&A, 501, 1269
Koleva, M., Prugniel, P., Bouchard, A., & Wu, Y. 2011, ULySS: A Full Spectrum Fitting Package, Astrophysics Source Code Library, ascl:1104.007

Korista, K. T., & Goad, M. R. 2004, ApJ, 606, 749
Kormendy, J., & Ho, L. C. 2013, ARA&A, 51, 511
Kourkchi, E., Courtois, H. M., Graziani, R., et al. 2020, AJ, 159, 67
Kriss, G. A., Mehdipour, M., Kaastra, J. S., et al. 2019, A&A, 621, A12
Magorrian, J., Tremaine, S., Richstone, D., et al. 1998, AJ, 115, 2285
Michell, J. 1784, RSPT, 74, 35
Netzer, H., & Marziani, P. 2010, ApJ, 724, 318
Onken, C. A., Ferrarese, L., Merritt, D., et al. 2004, ApJ, 615, 645
Pancoast, A., Brewer, B. J., & Treu, T. 2011, ApJ, 730, 139
Pancoast, A., Brewer, B. J., & Treu, T. 2014a, MNRAS, 445, 3055
Pancoast, A., Brewer, B. J., Treu, T., et al. 2014b, MNRAS, 445, 3073
Park, D., Kelly, B. C., Woo, J.-H., & Treu, T. 2012, ApJS, 203, 6

Patrick, A. R., Reeves, J. N., Lobban, A. P., Porquet, D., & Markowitz, A. G.
     2011, MNRAS, 416, 2725
Peterson, B. M. 1993, PASP, 105, 247
Peterson, B. M., Denney, K. D., De Rosa, G., et al. 2013, ApJ, 779, 109
Peterson, B. M., & Wandel, A. 1999, ApJL, 521, L95
Peterson, B. M., & Wandel, A. 2000, ApJL, 540, L13
Robinson, J. H., Bentz, M. C., Courtois, H. M., et al. 2021, ApJ, 912, 160
Skielboe, A., Pancoast, A., Treu, T., et al. 2015, MNRAS, 454, 144
Vazdekis, A., Sánchez-Blázquez, P., Falcón-Barroso, J., et al. 2010, MNRAS,
     404, 1639
Williams, P. R., Pancoast, A., Treu, T., et al. 2018, ApJ, 866, 75
Williams, P. R., Pancoast, A., Treu, T., et al. 2020, ApJ, 902, 74